Spreading of two–dimensional axisymmetric vortices exposed to a rotating strain field

By M. R. TURNER and A. D. GILBERT

Mathematics Research Institute, School of Engineering, Computing and Mathematics, University of Exeter, Exeter EX4 4QF, U.K.

This paper examines the evolution of an axisymmetric two–dimensional vortex in a steadily rotating strain field, and the dynamical interactions that can enhance vortex spreading through resonant behaviour.

Starting with a point vortex localised at the origin, the applied strain field generates a cat's eye topology in the co–rotating stream function, localised around a radius r_{ext}. Now the vortex is allowed to spread viscously: initially r_{ext} lies outside the vortex but as it spreads, vorticity is advected into the cat's eyes, leading to a local flattening of the mean profile of the vortex and so to enhanced mixing and spreading of the vortex. Together with this is a feedback: the response of the vortex to the external strain depends on the modified profile. The feedback is particularly strong when r_{ext} coincides with the radius r_{cat} at which the vortex can support cat's eyes of infinitesimal width. There is a particular time at which this occurs, as these radii change with the viscous spread of the vortex: r_{ext} moves inwards and r_{cat} outwards. This resonance behaviour leads to increased mixing of vorticity, along with a rapid stretching of vorticity contours and a sharp increase in the amplitude of the non–axisymmetric components.

The dynamical feedback and enhanced diffusion are studied for viscously spreading vortices by means of numerical simulations of their time evolution, parameterised only by the Reynolds number R and the dimensionless strength A of the external strain field.

---

1. Introduction

In this paper we explore the nonlinear evolution of a two–dimensional, coherent axisymmetric vortex within a steadily rotating, external strain field. Vortices commonly occur in atmospheric flows and idealised models such as two–dimensional turbulence, and are subject to external forcing.

There have been many previous studies examining the behaviour of a two–dimensional, forced vortex, for example in geophysical fluid dynamics where there is driving from the wind (Polvani and Plumb, 1992; Koh and Plumb, 2000; Thuburn and Lagneau, 1999) or in turbulent flows where the forcing is an irrotational flow arising from the interaction with other vortices in the flow (Moffatt *et al.*, 1994; Jiménez *et al.*, 1996; Bassom and Gilbert, 1998). Understanding how such vortical structures behave and respond to externally imposed strain fields in two–dimensional turbulence is important because they account for a large portion of the viscous dissipation of turbulent energy within the flow, while only occupying a tiny volume of the space (Hosokawa and Yamamoto, 1989). In atmospheric flows vortices are important for the transportation of fluid particles, chemicals and other pollutants (Provenzale, 1999). The southern polar vortex over Antarctica is continuously forced by wind currents flowing around the southern ocean, and this vortex

transports chemicals which break down the ozone layer, with environmental implications. This vortex also shows interesting features such as a 'surf zone', which is a region of well mixed fluid encircling a vortex core. Vortices exhibiting surf zones also arise in other atmospheric studies such as Thuburn and Lagneau (1999). These surf zones tend to form around a coherent core but sometimes the core undergoes a process of core splitting which has also been observed for the southern polar vortex (Charlton *et al.*, 2004).

Motivated by the presence of fine–scale vortices in three–dimensional turbulence, the study Moffatt *et al.* (1994) considers a three–dimensional vortex tube aligned along a positive strain axis of a steady strain field. Using the transformation of Lundgren (1982) this problem is converted into a two–dimensional one and an asymptotic theory is developed for large Reynolds numbers. The study finds that stretched vortex tubes can survive for long times even if one of the other strain axes is positive, provided the Reynolds number is large enough. A similar asymptotic method was later applied to a two–dimensional vortex in a weak steady strain field by Jiménez *et al.* (1996). Here the stream function possesses two hyperbolic points joined by dividing streamlines or separatrices: these separate an inner region of recirculating flow from the externally imposed strain field, which continues to infinity. Beyond these dividing streamlines, the asymptotic theory breaks down because vorticity is stripped at the hyperbolic points from the vortex to infinity. The effect of vortex stripping has been widely studied in relation to these strained vortex problems and is particularly important in turbulent flows (Dritschel and Waugh (1992); Dritschel (1995); Mariotti *et al.* (1994)). The results of Jiménez *et al.* (1996) agree well with simulations of two–dimensional turbulence.

While studies of steady external strain fields have been useful in understanding the basic structure of vortices in turbulence and geophysical flows, vortices are generally exposed to time–dependent strain fields. Our aim in this paper is to extend these studies to include the simplest form of time dependence in two dimensions, the case of a steadily rotating strain field, rotating with angular velocity α_{ext}. Having such a time–dependent strain adds two major features to the problem that are not in the steady strain problem. First, in a frame rotating with the external strain field, the corresponding steady stream function may now show a cat's eyes topology of the flow field, at a radius where fluid particles co–rotate with the strain (see figure 1). If the external strain field rotates with a fixed angular velocity α_{ext} then cat's eyes form at the critical radius $r = r_{\text{ext}}(t)$ (assuming in our discussion here that such a radius exists) where $\alpha(r_{\text{ext}}, t) = \alpha_{\text{ext}}$, writing $\alpha(r, t)$ as the angular velocity of the evolving vortex. (In fact as the external angular velocity tends to zero these cat's eyes open out to infinity, to leave the open topology in the study of Jiménez *et al.* (1996) described above. Or, to put it another way, any vorticity stripping for non–zero α_{ext} does not go to infinity, but simply recirculates in the cat's eyes.)

At the radius $r_{\text{ext}}(t)$, where the fluid particles co–rotate with the strain field and cat's eyes form, the azimuthal averaged profile is flattened (Turner and Gilbert, 2007), leading to enhanced mixing and an increased spreading of the vortex. This is largely a kinematic effect: cat's eyes are present when a circulating flow field and a rotating strain field are simply superposed. The second feature is more interesting, being dynamical: there now exists the possibility of resonance. A spreading vortex profile, such as a Gaussian case, has a particular radius $r_{\text{cat}}(t)$ at which inviscid cat's eyes of infinitesimal width can exist (Le Dizès, 2000). This radius is found by solving the inviscid linearized vorticity equation with a jump condition at the radius r. The value $r_{\text{cat}}(t)$ corresponds to the particular radius r where the resulting cat's eyes are quasi–steady. When the radius $r_{\text{cat}}(t)$ comes close to the externally forced radius $r_{\text{ext}}(t)$ there is a rapid feedback in the vorticity field generating high magnitude, non–axisymmetric components. This is expected to be particularly important when the strain field amplitude or Reynolds number is large.
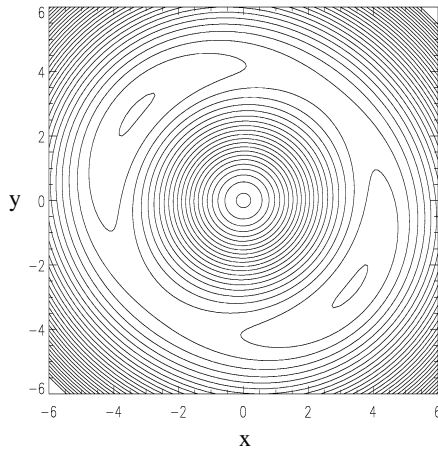
FIGURE 1. Schematic plot of the co–rotating stream function (3.2) for the vorticity profile $\omega = 1/(4\pi)e^{-r^2/4}$ superposing a rotating strain field with $\alpha_{\text{ext}} = 0.0089$ which generates cat's eyes at $r_{\text{ext}} = 4.22$.

To understand some of the aspects of vortices spreading in a time–dependent background field, this paper considers the fundamental problem of a viscously spreading two–dimensional vortex in a steadily rotating strain field. Initially we take a point vortex at the origin, and after non–dimensionalisation based on the vortex circulation and the angular velocity of the strain field, we are left with a problem containing just two parameters: the Reynolds number R and the strength of the strain field A. In terms of dimensional parameters, A corresponds to the ratio of the strain amplitude to its angular velocity α_{ext}. For the initial point vortex, the forcing gives a critical radius $r_{\text{ext}}(0)$ outside the vortex, and a value of $r_{\text{cat}}(0) = 0$. As the vortex spreads due to viscosity the vortex goes though a sequence of states where these radii move towards one another, $r_{\text{cat}}(t)$ increasing and $r_{\text{ext}}(t)$ decreasing, until the time when $r_{\text{ext}} \simeq r_{\text{cat}}$, where we will find a large resonant response of the vortex to the external strain.

This large external response also occurs in a linear framework: Lingevitch and Bernoff (1995) study the linear response of a fixed Gaussian vortex to an external strain, and vary the angular velocity α_{ext}. They observe a resonant response for which the linear non–axisymmetric perturbation amplitude peaks at one particular angular frequency, i.e. at one particular r_{ext} and corresponding α_{ext}. We will find results that agree with this study in cases of weak external strain amplitude. At higher amplitudes we are unable to fix our vortex profile as a Gaussian because the nonlinear interactions feed back to change our basic profile. However as our vortex spreads it explores the parameter space of external angular velocity versus vortex turnover time as is done in Lingevitch and Bernoff (1995), and models based on the Gaussian profile remain useful in interpreting our results.

The paper is laid out as follows. In §2 we give the governing equations, discuss the diagnostics used for monitoring the vortex evolution and the numerical scheme used in the simulations. In §3 we discuss the external strain field in more detail and in particular when we expect to see resonance in the vortex. In §4 and §5 we present the results of the nonlinear simulations. Section 4 examines the evolution for varying strain amplitude A in the cases $R = 10^3$, for which the vortex is relatively viscous, and $R = 10^4$. Section 5 considers $R = 10^5$ where the results become more inviscid: we see good agreement

between the resonance peak and the criterion $r_{\text{ext}}(t) = r_{\text{cat}}(t)$. Some concluding remarks and discussion are found in §6.

2. Formulation

We consider the vorticity equation in two–dimensional polar coordinates (r^*, θ),

$$\partial_{t^*}\omega^* + J(\omega^*, \psi^* + \psi_{\text{ext}}^*) = \nu\nabla^{*2}\omega^*, \quad \nabla^{*2}\psi^* = -\omega^*, \quad \nabla^{*2}\psi_{\text{ext}}^* = 0, \qquad (2.1)$$

where

$$r^*J(a,b) \equiv (\partial_{r^*}a)(\partial_\theta b) - (\partial_\theta a)(\partial_{r^*}b). \qquad (2.2)$$

The stars denote dimensional variables and ν is the kinematic viscosity. The $\psi_{\text{ext}}^*(r^*, \theta, t^*)$ term is an external irrotational strain field that has the form

$$\psi_{\text{ext}}^*(r^*, \theta, t^*) = \hat{A}r^{*m}e^{im(\theta - \alpha_{\text{ext}}t^*)} + \text{c.c.}, \qquad (2.3)$$

while the internal stream function ψ is taken to have no algebraic growth at infinity. This strain field has an $m-$fold symmetry in the θ–direction and constant amplitude $\hat{A}$, while its axes rotate with a constant angular velocity $\alpha_{\text{ext}} > 0$.

This paper focuses on the time evolution of a point vortex, with circulation $\Gamma > 0$, spreading viscously in the external strain field (2.3). Both rotate in the same direction, otherwise the problem is not very interesting as there are no cat's eyes generated. As the initial vortex has no length scale, the only parameters in the problem are Γ, ν, α_{ext} and $\hat{A}$. We non–dimensionalise by setting

$$t = \alpha_{\text{ext}}t^*, \qquad r = (\alpha_{\text{ext}}/\Gamma)^{1/2}\,r^*,$$

and the governing equations become

$$\partial_t\omega + J(\omega, \psi + \psi_{\text{ext}}) = R^{-1}\nabla^2\omega, \quad \nabla^2\psi = -\omega, \quad \nabla^2\psi_{\text{ext}} = 0, \qquad (2.4)$$

$$\psi_{\text{ext}}(r, \theta, t) = Ar^m e^{im(\theta - t)} + \text{c.c.}. \qquad (2.5)$$

Here $R = \Gamma/\nu$ is the Reynolds number based on the original total circulation and A is the dimensionless amplitude of the strain field, given by

$$A = \frac{\hat{A}}{\alpha_{\text{ext}}}\left(\frac{\alpha_{\text{ext}}}{\Gamma}\right)^{2-m}. \qquad (2.6)$$

For the case $m = 2$ the non–dimensional amplitude is simply the ratio of the dimensional strain amplitude to the dimensional strain frequency. The problem is parameterised by just two quantities (R, A), and can be thought of as a point vortex of unit circulation evolving in time t with a viscosity R^{-1} while exposed to a strain of unit angular velocity and amplitude A.

With no external strain field $(A = 0)$ the point vortex is subject only to viscous spreading, and is given by

$$\omega(r, t) = \frac{1}{4\pi L(t)^2}\,e^{-r^2/4L(t)^2}, \qquad L(t) = \sqrt{\frac{t}{R}}, \qquad (2.7)$$

where $L(t)$ is a characteristic length scale, the width of the vortex. For numerical purposes we have to start with a vortex of small but finite width L_0: the very early evolution of a spreading point vortex is unaffected by the external strain and so this is not a significant drawback. This is equivalent to beginning our simulation, not at $t = 0$ with a point vortex, but at the later time t_0, where $L_0 = (t_0/R)^{1/2}$. Our simulations thus run from $t = t_0$ and when we present our numerical results we will specify the value of t_0 used

for each Reynolds number; the quantity t is always the time after starting with a point vortex and we define $\tau = t - t_0$.

Starting with the initial axisymmetric vorticity field (2.7) for some given L_0, the external strain field with $m \neq 0$ distorts the vortex into a non–axisymmetric state. In the present work we shall consider the case $m = 2$, as $m = 1$ is a pure translation mode and this is of no dynamical interest. Although we only consider $m = 2$ here, we expect quantitatively similar results for $m > 2$. Because we cannot begin our numerical computations with a point vortex ($t_0 = 0$), we have an initial transient where the non–axisymmetric components of the vorticity increase in magnitude rapidly and oscillate. To stop this initial transient affecting our results we gradually switch on our forcing by using

$$A(t) = \begin{cases} A\sin(\pi t/(2T)) & \text{for } t < T, \\ A & \text{for } t > T, \end{cases} \tag{2.8}$$

where T is some given time. Extensive testing has shown that results with the forcing (2.8) are in excellent agreement with those where t_0 has been made as low as computationally possible so that the initial transient is small.

The evolution of $\omega(r, \theta, t)$ and $\psi(r, \theta, t)$ is then found by time–stepping (2.4), where we seek a solution in the form of a truncated sum of Fourier harmonics

$$\omega(r, \theta, t) = \sum_{k=-N}^{N} \omega_{mk}(r, t) e^{imk\theta}, \quad \psi(r, \theta, t) = \sum_{k=-N}^{N} \psi_{mk}(r, t) e^{imk\theta}.$$

The external strain field ψ_{ext} in (2.5) drives the $m = 2$ mode of the vorticity field which then excites higher Fourier harmonics, as well as modifying the basic profile ω_0 via the nonlinear terms $J(\omega, \psi + \psi_{\text{ext}})$ of (2.4). To integrate (2.4) we use the Crank–Nicholson method on the linear terms and the second order Adams–Bashforth method on the nonlinear terms. The discretisation in the radial direction uses a finite difference method with M grid points in the range $0 \leq r \leq r_0$. The Poisson equation for ψ in (2.4) is solved for $\psi(r, \theta, t)$ by inverting a tridiagonal matrix system. The code uses N Fourier harmonics and for this study typical resolution values are $(N, M, r_0) = (128, 1500, 6)$ for $R = 10^3$ and 10^4 while $(N, M, r_0) = (128, 1500, 1.5)$ for $R = 10^5$.

In order to measure the response of the vortex we define the jth multipole moment of the vorticity field as

$$Q_j(t) = \int_0^\infty r^j \omega_j(r, t) \, r \, dr \quad (j \geq 1),$$

which is related to the far–field form of the (internal) stream function via $2j\psi_j \sim Q_j(t)r^{-j}$ as $r \to \infty$. To quantify the effect of the strain field on the vortex we consider the following diagnostics: the value of the vorticity field at the origin $\omega_{\text{or}}(t) \equiv \omega(0, \theta, t)$ and the width of the vortex, $\sigma(t)$, which we define as

$$\sigma = \frac{1}{\sqrt{\pi}} \int_0^{2\pi} \int_0^\infty r\omega(r, t) \, r \, dr \, d\theta = 2\sqrt{\pi} \int_0^\infty r^2 \omega_0(r, t) \, dr.$$

When there is no external strain field, $A = 0$, the quantities $\omega_{\text{or}}(t)$ and $\sigma(t)$ are, from (2.7),

$$\omega_{\text{or}}(t) = R/4\pi t, \qquad \sigma(t) = (t/R)^{1/2}. \tag{2.9}$$

Before we present the results of the simulations, we first discuss the critical layer introduced by the strain field and discuss further how a resonant response can occur in the vortex.

3. Resonant behaviour from inviscid theory

Consider an axisymmetric vortex with an azimuthally averaged vorticity profile $\omega_0(r,t)$ in the external strain field (2.5) rotating with angular velocity α_{ext}. (In non–dimensional variables $\alpha_{\mathrm{ext}} = 1$, but it is more intuitive to leave α_{ext} general in this discussion section). This axisymmetric vortex has the angular velocity

$$\alpha(r,t) = \frac{1}{r^2} \int_0^r \omega_0(s,t)\, s\, ds,$$

which for the diffusing point vortex profile given in (2.7) is

$$\alpha(r,t) = \frac{1}{2\pi r^2} \left(1 - e^{-r^2/4L(t)^2} \right).$$

First for simplicity we focus on a fixed vortex, a Gaussian vortex with $L(t) = 1$, and ignore viscous spreading and other time–dependence. With no external forcing present ($A = 0$), there is a single radius at which infinitesimally thin, steadily rotating, inviscid cat's eyes can persist (Le Dizès, 2000): we denote this radius by r_{cat}, for which the corresponding angular velocity is α_{cat} given by $\alpha(r_{\mathrm{cat}}) = \alpha_{\mathrm{cat}}$, and we have

$$r_{\mathrm{cat}} \simeq 3.44, \quad \alpha_{\mathrm{cat}} \simeq 0.0127 \qquad (L(t) = 1). \tag{3.1}$$

The radius r_{cat} is calculated by solving a linear problem with a jump condition at the critical radius r_{cat}; the jump captures information from a critical layer, in which there is an inner, inviscid, nonlinear solution of cat's eyes on a smaller length–scale (Le Dizès, 2000). The particular radius $r_{\mathrm{cat}}(t)$ occurs when the corresponding mode to the linearized equation is neutral. This study was extended by Turner *et al.* (2008) to include finite thickness cat's eyes by calculating the corresponding Landau pole of the azimuthal averaged profile $\omega_0(r,t)$ (Briggs *et al.*, 1970; Turner and Gilbert, 2007). In short, the vortex has a natural inviscid, 'resonant' radius r_{cat}.

Inviscid, thin cat's eyes can exist at other radii but to be sustained these require a non–zero external forcing amplitude $A \neq 0$. A strain field of angular frequency α_{ext} produces a critical layer at $r = r_{\mathrm{ext}}$ which satisfies $\alpha(r_{\mathrm{ext}}) = \alpha_{\mathrm{ext}}$ (provided a solution r_{ext} exists). Here the fluid particles of the vortex co–rotate with the strain field and a cat's eye topology forms in the co–rotating stream function

$$\psi_{\mathrm{co}}(r,\theta,t) = \psi(r,\theta,t) + \tfrac{1}{2}\alpha_{\mathrm{ext}} r^2; \tag{3.2}$$

by advection this subsequently generates cat's eye features in the vorticity field. One key question is what is the effective Reynolds number R_{eff} in the cat's eyes? As these have a scale of order $A^{1/2}$ and turnover time scale of order $A^{-1/2}$, the quantity R_{eff} could be rather smaller than the nominal R. The sensible definition is

$$R_{\mathrm{eff}} = A^{3/2} R, \tag{3.3}$$

which is essentially the inverse of the Haberman parameter of Le Dizès (2000) (also see Haberman (1972)). This definition also arises in the critical layer analysis of Hall *et al.* (2003). When the external frequency is tuned so that $r_{\mathrm{cat}} = r_{\mathrm{ext}}$ at large R_{eff}, there is a resonance effect and the non–axisymmetric perturbation vorticity has a large increase in amplitude.

With viscosity, that is for moderate or small R_{eff} but $R \gg 1$, again a non–zero external amplitude A is required to sustain cat's eyes at any radius, and the radius of peak response moves outwards slightly from r_{cat} with increasing viscosity. This resonance was seen in the study of Lingevitch and Bernoff (1995) who considered linear perturbations to the profile (2.7) with $L(t) = 1$. These authors found that a peak in the perturbation vorticity
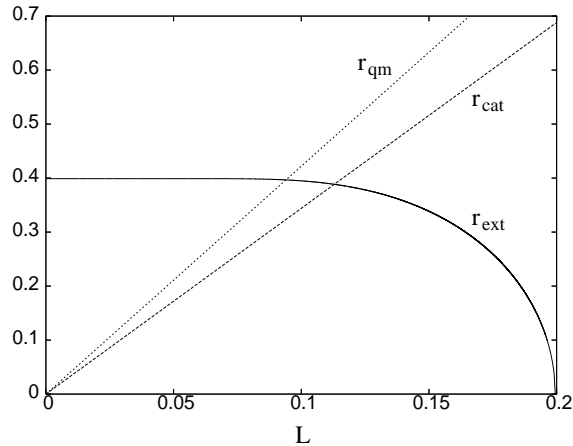
FIGURE 2. Plot of r_{ext} (solid), r_{cat} (dashed) and r_{qm} (dotted) as functions of L for the profile (2.7) and $\alpha_{\text{ext}} = 1$. Both the cat's eye radius ($r_{\text{cat}} = 3.44L$) and the quasi–mode radius ($r_{\text{qm}} = 4.22L$) are linear functions of L.

does exist and that in the limit $R \to \infty$ this peak occurs at

$$r_{\text{ext}} = 3.69, \quad \text{with} \quad \alpha_{\text{ext}} = 0.0113, \tag{3.4}$$

for this value of L. This is different from the values of r_{cat} and α_{cat} given in (3.1), and the reason is that even though this result is obtained in the limit $R \to \infty$, linearisation corresponds to $A \to 0$ with $R_{\text{eff}} \to 0$: thus the results correspond to forced, highly viscous cat's eyes. Taking viscosity into account Le Dizès (2000) determined the resonant value in (3.4) with an error of less than 0.1%.

Having discussed cat's eyes on a fixed Gaussian profile with $L(t) \equiv 1$ we now restore the viscous spreading and use the discussion above of the inviscid case as a guide. We will find that the behaviour at a given time t with a given $L(t)$ is linked to the above case with $L(t)$ appropriately rescaled, and observe increasing improvement at larger Reynolds numbers. If we consider the diffusing Gaussian solution in (2.7) then we can calculate both r_{cat} and r_{ext} for varying $L(t)$: the value where these agree should give us an estimate for the value of L at which resonance will occur. To calculate r_{ext} we require the solution of

$$\frac{1}{2\pi r_{\text{ext}}^2} \left(1 - e^{-r_{\text{ext}}^2/4L^2} \right) = \alpha_{\text{ext}}$$

for a given value of L, which is found using an interval halving iterative scheme for a particular α_{ext}. To calculate r_{cat} we use the numerical method of Le Dizès (2000), and we plot both r_{cat} and r_{ext} as a function of L in figure 2 for $\alpha_{\text{ext}} = 1$. The radius r_{cat} is linear in L and has the form $r_{\text{cat}} = 3.44L$, while $r_{\text{ext}} = 1/(2\pi\alpha_{\text{ext}})^{1/2}$ at $L = 0$ and vanishes when $L = 1/(8\pi\alpha_{\text{ext}})^{1/2}$. After this point a resonant radius connected to the existence of cat's eyes ceases to exist.

From figure 2 we see that r_{cat} and r_{ext} cross when $L_{\text{cat}} \simeq 0.113$ and $r_{\text{cat}} = r_{\text{ext}} \simeq 0.389$. This result suggests that in our simulations we should see resonant effects when $\omega_{\text{or}} = \omega_{\text{cat}}$ and $\sigma = L_{\text{cat}}$ from (2.9). In summary this is

$$\sigma = L_{\text{cat}} \simeq 0.113, \quad r_{\text{cat}} = r_{\text{ext}} \simeq 0.389, \quad \omega_{\text{cat}} = \omega_{\text{or}} \simeq 6.23. \tag{3.5}$$

The discussion in the paragraph immediately above, together with figure 2 is strictly only valid for inviscid, infinitesimally thin cat's eyes in the limits $A \to 0$, $R_{\text{eff}} \to \infty$, by Le Dizès (2000). We are solving an initial problem numerically and while in theory

such cat's eyes may emerge cleanly in the limit $t \to \infty$ for a run with $R_{\text{eff}} \gg 1$ and $A \ll 1$, such runs are extremely difficult to perform (though see the development of cat's eyes in the asymptotic model of Balmforth *et al.*, 2001). Nonetheless the resonance phenomenon is real and the above discussion gives a useful guide as to the phenomena we may expect in our simulations of viscously spreading vortices subject to an applied external forcing. Although our discussion is for cat's eyes, on a Gaussian profile, that are inviscid $R_{\text{eff}} \to \infty$, and have infinitesimal width, $A \to 0$, we will find the above thresholds to be approximately correct for viscous, finite thickness cat's eyes on the profiles that are not always very close to Gaussian, particularly near the vortex periphery. The work of Lingevitch and Bernoff (1995), shows that for finite effective Reynolds numbers R_{eff} the position of the peak perturbation vorticity values moves to smaller angular velocities, i.e. to larger radii, for a Gaussian profile. On the other hand Turner *et al.* (2008) show that if the cat's eyes have finite thickness, then the position of r_{cat} moves to smaller radii. However for both of these studies the deviation of the radius from the inviscid result is small, and so the inviscid analysis gives useful guidance. In fact given that our simulations have a profile evolving with time and possessing more complex structure, it would be impossible to pin down these effects precisely in any case.

Along with r_{ext} and r_{cat} there is a third radius of interest to us as a point of comparison, which we call r_{qm}. This radius is the 'quasi–mode' radius of the vortex profile. A quasi–mode is essentially a wave located in the core of a vortex and, although it appears as a single mode, it is in fact more accurate to characterize it as a wave packet of continuum modes. The quasi–mode itself is a solution of the linearized Euler equations which is not separable in time and it decays exponentially on a time–scale that is much longer than the turn–over time–scale of the underlying vortex; together with decay it possesses a frequency α_{qm} that corresponds to the radius r_{qm} through $\alpha_{\text{qm}} = \alpha(r_{\text{qm}})$ (Briggs *et al.*, 1970; Schecter *et al.*, 2000; Turner and Gilbert, 2007). For the Gaussian vortex (2.7), it can been calculated that $r_{\text{qm}} \simeq 4.22L$ while the corresponding $\alpha_{\text{qm}} = 0.0089L^{-2}$. The radii r_{cat} and r_{qm} for the profile (2.7) are plotted in figure 2. The corresponding values for a resonance between the external frequency and the quasi–mode, $r_{\text{qm}} = r_{\text{ext}}$, are given by

$$\sigma = L_{\text{qm}} \simeq 0.094, \quad r_{\text{qm}} = r_{\text{ext}} \simeq 0.397, \quad \omega_{\text{qm}} = \omega_{\text{or}} \simeq 9.01. \tag{3.6}$$

These are not far from those for the resonance with inviscid cat's eyes in (3.5). Note that in the limit of a compact vortex, for example a Rankine vortex, with weak vorticity outside, the two radii r_{qm} and r_{cat} coincide (Balmforth *et al.*, 2001; Le Dizès, 2000), but for general profiles they are distinct.

4. Results for $R = 10^3$ and $R = 10^4$

In the next two sections we present results from our numerical simulations. In this section we start by considering the moderate Reynolds numbers of $R = 10^3$ and $R = 10^4$. In the $R = 10^3$ case, viscosity rapidly destroys any fine scale structures that form in the vorticity field, and the vortex itself quickly spreads, while in the $R = 10^4$ case we are better able to study the critical layer interactions as the vortex spreads more slowly. We group together the $R = 10^3$ and 10^4 cases as the phenomena observed are similar. However the picture becomes more complex at larger Reynolds numbers and we examine the vortex evolution in more detail for $R = 10^5$ in §5 where the diffusion rate is very slow and our simulations are approaching the inviscid limit. For the values of R considered in this section, the simulations are started with the vorticity profile given by (2.7) with
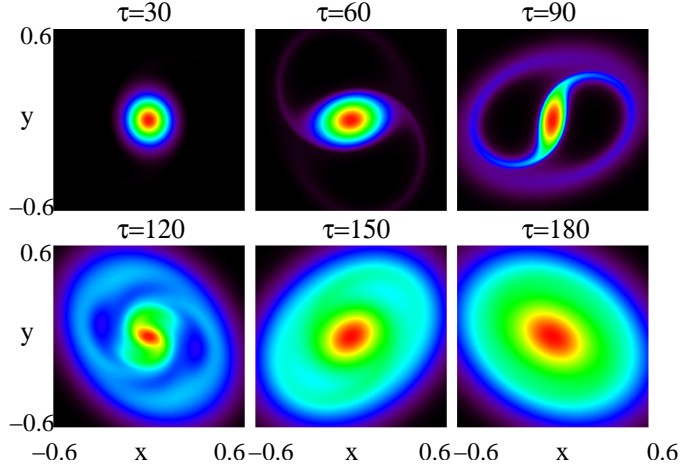
FIGURE 3. Plot of $\omega(r,\theta,t)$ for the case $R = 10^4$ and $A = 0.05$ at times $\tau = 30$, 60, 90, 120, 150 and 180 with $t_0 = 9$. Red indicates regions of high vorticity and black regions of low vorticity. Note in each panel the vorticity is rescaled so red indicates the maximum vorticity of that panel.

$L_0 = 0.03$ for $R = 10^3$ and $L_0 = 0.04$ for $R = 10^4$. Our simulations thus commence at $t_0 = 0.9$ for $R = 10^3$ and at $t_0 = 16$ for $R = 10^4$.

4.1. *Moderate forcing amplitude* $A = 0.05$

We begin with a strain field with strength $A = 0.05$ which is moderate, in the middle of the range we study. Figure 3 plots the vorticity field, $\omega(r,\theta,t)$, for this case and $R = 10^4$ at time intervals $\tau = t - t_0$ from 30 to 180 in increments of 30. This process is reasonably viscous with $R_{\text{eff}} \simeq 112$. At early times, $\tau = 30$, the vortex spreads as a point vortex would do in the absence of an external strain field. However by $\tau = 60$ the forcing has become significant: two spiral arms of vorticity have been pulled out and are wrapping up into cat's eyes around an elongated elliptical core. By $\tau = 90$ the core is now very elongated and the filaments have reconnected with the vortex giving a 'halo' effect around the vortex, encasing the cat's eyes. At $\tau = 120$ we can see the vorticity from the core spreading rapidly to fill the space between the coherent core and the halo region. Beyond this time it is difficult to see any dynamical effects in the vorticity field and the vortex now appears as a diffusing elliptical vortex. However we can gain more qualitative information by considering plots of both $\omega_0(r,t)$ and $|\omega_2(r,t)|$ for this case and the $R = 10^3$ case.

Figures 4 and 5 plot (a) profiles $\omega_0(r,t)$ and (b) components $|\omega_2(r,t)|$ for $R = 10^3$ and 10^4 respectively, at a sequence of times with the linestyles given in the captions. For $R = 10^3$ in figure 4(a) $\omega_0(r,t)$ has a clear flat region for $\tau = 10$ (solid line) at $r \simeq 0.5$, and for $\tau = 20$ (dotted line) the profile has a weak tendency to flatten at $r \simeq 0.35$. These deformations correspond to the existence of spiral filaments similar to those in figure 3 (except smaller), and a large value of $|\omega_2(r,t)|$ in figure 4(b). Beyond this time $\omega_0(r,t)$ appears as a diffusing Gaussian, and as the maximum value of $|\omega_2(r,t)|$ decays so the vortex axisymmetrizes.

However for $R = 10^4$, $\omega_0(r,t)$ in figure 5(a) for the early time (solid line) appears almost Gaussian while $|\omega_2(r,t)|$ in figure 5(b) has a hump with the peak at $r \simeq 0.12$. At $\tau = 60$ (dotted line), when spiral filaments are observed in the vorticity field, $\omega_0(r,t)$ has a region of homogenized vorticity between $r \simeq 0.4$ and $r \simeq 0.6$ which is approximately the region of the cat's eyes in figure 3. This flattening is accompanied by an increase of
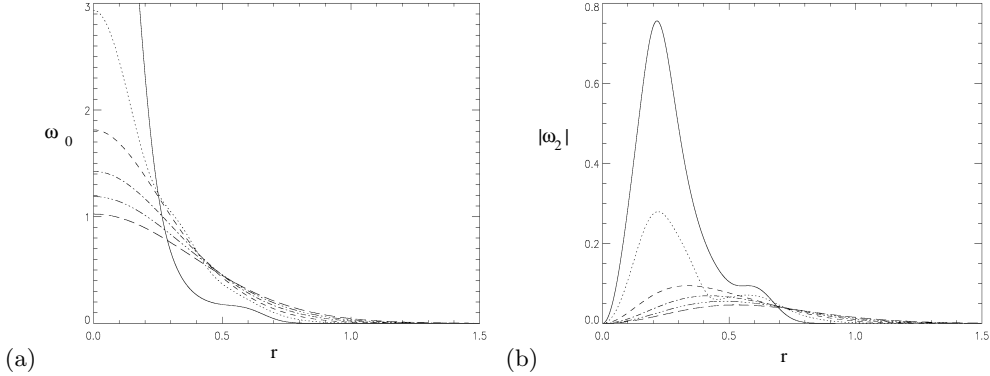
FIGURE 4. Plot of (a) $\omega_0(r,t)$ and (b)$|\omega_2(r,t)|$ against r for the case $R = 10^3$ and $A = 0.05$ at times $\tau = 10$ (solid), 20 (dot), 30 (dash), 40 (dot–dash), 50 (triple–dot–dash) and 60 (long dash) with $t_0 = 0.9$.
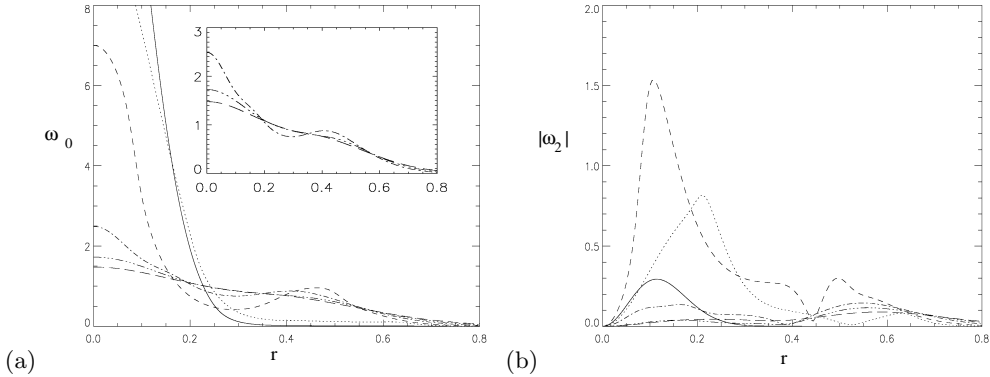

FIGURE 5. Plot of (a) $\omega_0(r,t)$ and (b) $|\omega_2(r,t)|$ against r for the case $R = 10^4$ and $A = 0.05$ at times $\tau = 30$, 60, 90, 120, 150 and 180 with $t_0 = 16$ and the same line style order as figure 4. The insert in panel (a) shows the $\tau = 120$, 150 and 180 results separately for clarity.

the peak in $|\omega_2(r,t)|$ at $r \simeq 0.20$. As time increases to $\tau = 90$ (dashed line) $\omega_0(r,t)$ in figure 5(a) overturns and gains a second peak at $r \simeq 0.47$ as the critical layer of the strain field, r_{ext}, moves towards $r = 0$, and $|\omega_2(r,t)|$ reaches its maximum value at $r \simeq 0.1$. The vorticity then spreads rapidly and $\omega_0(r,t)$ has a profile with a small flattened region at $r \simeq 0.35$ for $\tau = 150$ and 180. At these times $|\omega_2(r,t)|$ has a broad peak structure, lower in value much like the $R = 10^3$ case, and the vortex spreads and axisymmetrizes.

At this point, the comparison with the resonance values, in particular (3.5), is somewhat unclear: however in figure 5(b) the ω_2 harmonic does develop a clear large peak at a radius $r \simeq 0.1$ at time $\tau = 90$, which is linked to the formation of cat's eyes. To clarify this, we reduce the amplitude A in the next subsection.

4.2. *Weak forcing amplitude $A = 0.001$*

Before looking at further diagnostics and aspects of resonance, we reduce the forcing amplitude, so as to compare profiles with the linear results of Lingevitch and Bernoff (1995) for a Gaussian vortex. We consider the forcing amplitude $A = 0.001$ for $R = 10^4$ and plot $\omega_0(r,t)$ and $|\omega_2(r,t)|$ from $\tau = 30$ to 180 in increments of 30 as shown in figures 6(a) and 6(b) respectively. Because A is small, $\omega_0(r,t)$ appears to be just a decaying
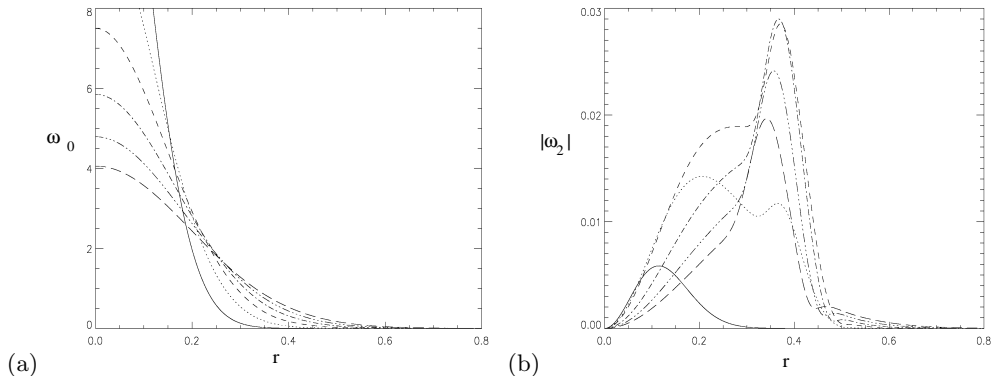
FIGURE 6. Plot of (a) $\omega_0(r,t)$ and (b) $|\omega_2(r,t)|$ against r for the case $R = 10^4$ and $A = 0.001$ at times $\tau = 30$, 60, 90, 120, 150 and 180 with $t_0 = 16$ and the same line style order as figure 4.

Gaussian vortex with no visible defects in its appearance, as is reflected in vorticity field plots (not shown).

The interesting feature in this figure is the behaviour of $|\omega_2(r,t)|$. At $\tau = 30$ (solid line) $|\omega_2(r,t)|$ has a single peak structure, with the peak maximum at $r \simeq 0.1$. However as t increases a second peak emerges around $r \simeq 0.37$, and by $\tau = 90$ this peak is now dominating $|\omega_2|$. This second peak reaches its maximum value between $\tau = 90$ (dashed line) and $\tau = 120$ (dot–dashed line) while the first peak has now disappeared completely by $\tau = 120$. This second peak then slowly decays away beyond this point. This second peak is the resonant effect of the strain field and we expect this to be important once the amplitude of the forcing reaches some critical value. The fact that $|\omega_2|$ is not close to zero in the range $0.1 < r < 0.25$, say, shows that as well as exciting the critical layer, the forcing also significantly distorts the vortex core, akin to a normal mode on a Rankine vortex (see Balmforth *et al.*, 2001).

The shape of $|\omega_2(r,t)|$ in figure 6(a) agrees well with the linear study of Lingevitch and Bernoff (1995). The agreement is not perfect, but this is unsurprising: as discussed earlier, $R_{\text{eff}} \to 0$ in the linear viscous limit, while for the results presented here $R_{\text{eff}} = 0.316$ which is not particularly small. We conclude that the secondary peak for $A = 0.001$ in figure 6(b), and that for $A = 0.05$ in figure 5(b), are the same phenomenon, namely the resonance of the external forcing and the cat's eyes generated within the vortex.

4.3. *Time development of $\omega_{\text{or}}(t)$ for all amplitudes*

For a view of the continuous time development, rather than snapshots of profiles, figures 7(a) and 8(a) plot the value of the vorticity at the origin ω_{or} against $\tau = t - t_0$ for $A = 0$, 0.001, 0.01, 0.05, 0.1 and 0.15 labelled 1–6, for $R = 10^3$ and $R = 10^4$ respectively. The corresponding values of R_{eff} go from 0.0316 to 58.1 for $R = 10^3$ and 0.316 to 581 for $R = 10^4$ (excluding the $A = 0$ result). The right panels, figures 7(b) and 8(b) show the same results on a log–log scale.

We can see three regimes, mostly clearly in figures 7(b) and 8(b): an initial regime of the point vortex spreading, followed by a window of dynamical interaction between the strain and the vortex, and then a final regime of the vortex again spreading with a power law dependence. Our focus is the second, dynamical window, roughly $5 < \tau < 30$ for $R = 10^3$ and $50 < \tau < 150$ for $R = 10^4$. It is here that vorticity spreads into the cat's eyes generated by the external field and the vorticity profile is changed significantly, with dynamical feedback effects.
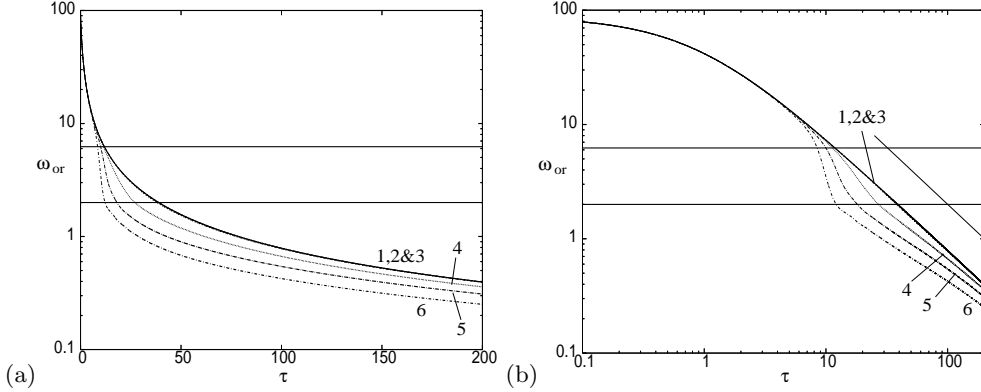
FIGURE 7. Plot of (a) $\omega_{\rm or}$ against τ for the case $R = 10^3$ and $A = 0$, 0.001, 0.01, 0.05, 0.1 and 0.15 numbered 1 to 6 respectively. Panel (b) is the same as panel (a) on a log–log plot. The upper horizontal line corresponds to the resonant value $\omega_{\rm or} = \omega_{\rm cat}$, the lower horizontal line corresponds to the cat's eyes disappearing and the other straight line in (b) is proportional to τ^{-1}.
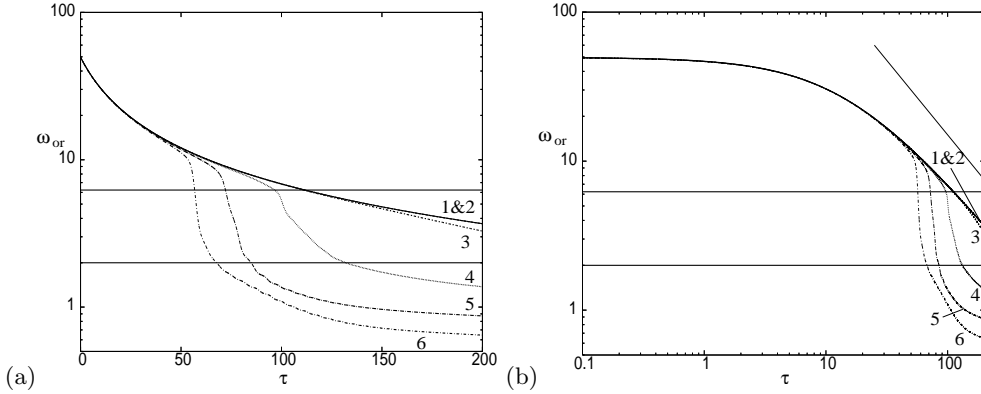

FIGURE 8. Plot of (a) $\omega_{\rm or}$ against τ for the case $R = 10^4$ and $A = 0$, 0.001, 0.01, 0.05, 0.1 and 0.15 numbered 1 to 6 respectively. Panel (b) is the same as panel (a) on a log–log plot. The upper horizontal line corresponds to the resonant value $\omega_{\rm or} = \omega_{\rm cat}$, the lower horizontal line corresponds to the cat's eyes disappearing and the other straight line in (b) is proportional to τ^{-1}.

In both figures the $A = 0$ curve represents the analytical result $\omega_{\rm or} = R/4\pi t$ given in (2.9) and the upper horizontal line gives the value of $\omega_{\rm or} = \omega_{\rm cat} = 6.23$ from (3.5) at which we predict a resonance effect when $r_{\rm ext} = r_{\rm cat}$ from the inviscid theory in §3. The corresponding value of $\omega_{\rm or}$ for the other possible resonance with the quasi–mode, $r_{\rm ext} = r_{\rm qm}$, is $\omega_{\rm or} = \omega_{\rm qm} \simeq 9.01$ from (3.6). For both values of the Reynolds number the result for $A = 0.001$ (curve 2) is indistinguishable from the $A = 0$ (curve 1) result. However as A is increased we see that $\omega_{\rm or}$ begins to decay faster at early times showing a greater rate of diffusion of the core of the vortex.

For $R = 10^3$, the largest values of A give a vorticity value at the origin which drops very rapidly and then levels out to a decay proportional to τ^{-1} for longer times. This decay rate is the same as for the $A = 0$ case, which is to be expected as Rhines and Young (1983) show that an elliptical patch of scalar spreads in a similar manner to a circular patch with vorticity essentially constant on streamlines and an increased effective diffusivity. This is because the stream function in a suitable co–rotating frame will be
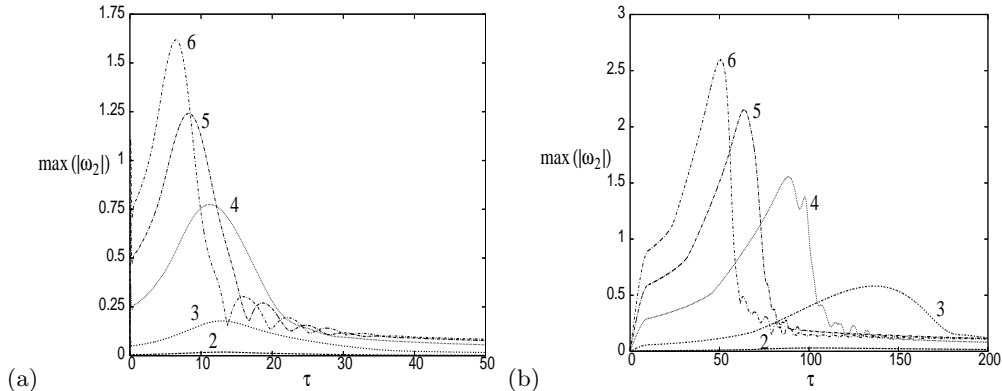
FIGURE 9. Plot of $\max(|\omega_2|)$ against τ for (a) $R = 10^3$ and (b) $R = 10^4$ for $A = 0.001$, 0.01, 0.05, 0.1 and 0.15 numbered 2 to 6 respectively.

steady and vorticity rapidly homogenised on its contours. This power–law decay can be seen more clearly in the log–log plot in 7(b) by comparing with the line giving the slope τ^{-1}.

As A is increased for the $R = 10^4$ case in figure 8(a) we see a clear trend emerging in the $\omega_{\rm or}(t)$ results. In this case the vortex now spreads more slowly, because of the decreased viscosity: the key effect is to open out the dynamical window, with a higher effective Reynolds number $R_{\rm eff}$, in the range 0.316 to 581, characterising the motions in the cat's eyes that form. At the start of the dynamical window the rapid decay seen for $R = 10^3$ is present and enhanced, particularly at the larger values of A up to the $A = 0.15$ case where the downwards gradient of $\omega_{\rm or}$ is very large. Comparing figure 8 with figure 3 we note that the homogenization of the vorticity in the cat's eyes occurs at approximately the same time as the rapid drop in $\omega_{\rm or}(t)$.

We can now compare the time at resonance with the value when $\omega_{\rm or} \simeq \omega_{\rm cat}$ predicted, namely that in (3.5), and given by the upper horizontal lines in the two panels of figures 7 and 8. In both figures there is a reasonable qualitative agreement, and in particular for $R = 10^4$ in figure 8 with $A = 0.05$ (curve 4) this resonant value agrees well with the onset of the rapid drop in $\omega_{\rm or}$ from the feedback of nonlinear terms. The discrepancy for larger values of A can be accounted for by the fact that in these cases the critical layer is wider and also the basic profile $\omega_0(r,t)$ has been modified by the strain field, so the values of $r_{\rm qm}$ and $r_{\rm ext}$ have also changed: this is something we will take up in the next section as we increase the Reynolds number to $R = 10^5$. At this Reynolds number it is not clear if the quasi–mode radius defined in (3.5) is significant in the resonant behaviour of the vortex because $\omega_{\rm or} = \omega_{\rm qm} \simeq 9.01$ appears within the dynamical window for the three largest amplitude forcings. However in §4.4 and in §5 we shall see that this radius is not significant and we confirm that it is $r_{\rm cat}$ which is the resonant radius. It is worth noting here that from §3 we know that the critical radius vanishes when $L^2 = 1/8\pi$ (with $\alpha_{\rm ext} = 1$) which means that cat's eyes vanish from the co–rotating stream function when $\omega_{\rm or} \simeq 2$. Thus we observe in figures 7(a) and 8(a) that there is a sudden, albeit slight, change in the gradient of $\omega_{\rm or}$ at this value signifying the vanishing of the cat's eyes.

4.4. *Time development of other diagnostics*

Of our diagnostics, we have obtained the most agreement with theory from the value of the vorticity at the origin $\omega_{\rm or}(t)$, which is discussed in the previous section. In this section we consider the time evolution of the maximum value of ω_2, $\max(|\omega_2|)$, which
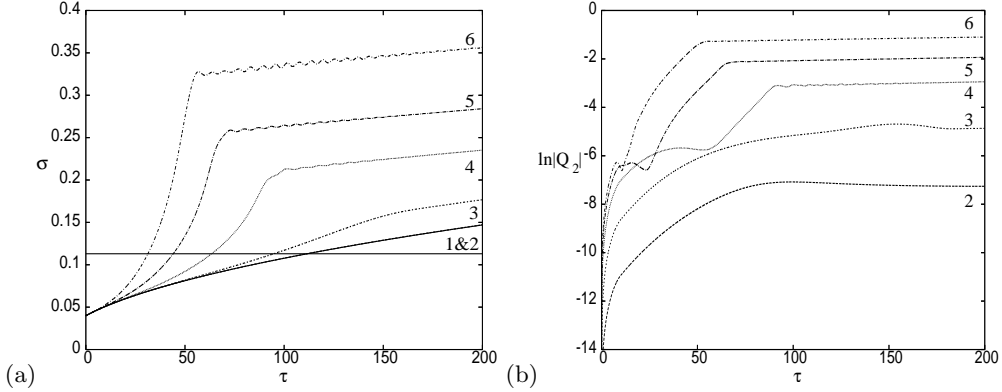
FIGURE 10. Plot of (a) $\sigma(t)$ for $R = 10^4$ and $A = 0$, 0.001, 0.01, 0.05, 0.1 and 0.15 numbered 1 to 6 respectively. Panel (b) plots $\log |Q_2(t)|$ for the same values of A except $A = 0$. The horizontal line corresponds to the resonant value (3.5).

also agrees well with the theory, and the other diagnostics, the width $\sigma(t)$ and far field amplitude $Q_2(t)$ which are less informative.

In figure 9 we plot the evolution of $\max(|\omega_2|)$ for $A = 0$, 0.001, 0.01, 0.05, 0.1 and 0.15 with the same line numbering as in figures 7 and 8 for (a) $R = 10^3$ and (b) $R = 10^4$ respectively. For $R = 10^3$ we see that $\max(|\omega_2|)$ rises to a maximum value before decaying for larger times. This maximum value occurs at a time which agrees well with the time when $\omega_{\text{or}} = \omega_{\text{cat}}$ in figure 7. For the two largest forcing values, there exist oscillations in $\max(|\omega_2|)$ which occur after the decay of the initial maximum. This is due to a feedback from the higher Fourier modes advecting vorticity around the cat's eyes, which becomes more pronounced as R increases. The corresponding figure for $R = 10^4$ in figure 9(b) has very similar features. For $\tau < 10$ we see an increase in the value of $\max(|\omega_2|)$ as the forcing is gradually switched on. Then, for the largest forcing amplitudes (lines 4, 5 and 6), we see a kink in this diagnostic before the maximum value occurs. This kink occurs when the second peak in $|\omega_2|$ (see figure 6(b)) becomes large enough so that it is now the dominant peak in $|\omega_2|$ and hence the value determined by $\max(|\omega_2|)$. Again the maximum value of $\max(|\omega_2|)$ agrees well with the time when $\omega_{\text{or}} = \omega_{\text{cat}}$ in figure 8, but in this case the feedback oscillations are also observed in the $A = 0.05$ result as well as for larger values of A.

Figure 10(a) plots $\sigma(t)$ for $A = 0$, 0.001, 0.01, 0.05, 0.1 and 0.15 with the same line numbering as in figure 8 for $R = 10^4$. This figure shows that as the value of $\omega_{\text{or}}(t)$ drops rapidly (see figure 8(a)) the width of the vortex $\sigma(t)$ increases rapidly. The rapid increase in $\sigma(t)$ ends once the cat's eyes have vanished from the vortex (approximately equal to the time when $\omega_{\text{or}} \simeq 2$), and then σ grows like $\sigma \propto t^{1/2}$ for large times. However we observe that the largest forcing values give a σ which oscillates for a period of time before settling down to a smooth growth for large times. This pulsation of the vortex is a result of the basic vorticity profile being rearranged as a large amount of vorticity spreads into the cat's eyes, shown in figure 4(a).

Figure 10(b) plots $\log |Q_2(t)|$ for the same values of A (except $A = 0$) as in panel 10(a) for $R = 10^4$. We see that for each value of A, $|Q_2|$ rapidly rises in value reaching a peak around the same time as $\omega_{\text{or}} = \omega_{\text{cat}}$ in figure 8(a). After this rise, $|Q_2(t)|$ then decays slightly before ultimately growing slowly in time. This final regime of slow growth corresponds to the slow propagation of the $|\omega_2(r, t)|$ peak to larger values of r, as shown
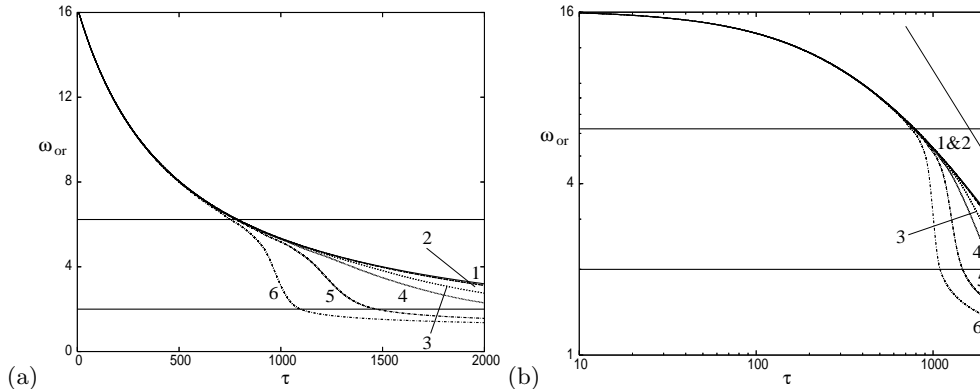
FIGURE 11. Plot of ω_{or} against τ with $t_0 = 490$ for the case $R = 10^5$ and $A = 0$, 0.001, 0.0025, 0.005, 0.01 and 0.02 numbered 1 to 6 respectively. Panel (b) plots the same results on log–log scales. The upper horizontal line corresponds to the resonant value $\omega_{\text{or}} = \omega_{\text{cat}}$, the lower horizontal line corresponds to the cat's eyes disappearing and the other straight line in (b) is proportional to τ^{-1}.

in figure 4(b). The large values of A have a secondary increase in $|Q_2|$ which ends at the time when $\sigma(t)$ stops its rapid increase in figure 10(a).

The results presented in this section for $R = 10^3$ and 10^4 highlight the presence of the dynamical window of interaction between vortex and external strain. The picture is not entirely clear though: as the vortex spreads outwards, it passes through this window quite quickly. It is therefore only at the stronger forcing amplitudes that we see strong interactions. Having discussed these cases we are ready to open up the dynamical window wider by considering simulations with $R = 10^5$.

5. Results for $R = 10^5$

In this section we examine how the strain field affects the point vortex in a more inviscid situation with $R = 10^5$. The aim of this section is to extend the time period where the vortex has dynamical interactions so we can understand the phenomena of the rapid drop of ω_{or} seen in §4.

5.1. *Time development of diagnostics for all amplitudes*

For $R = 10^5$ the viscous decay of the vortex occurs so slowly, on a time scale of $O(R)$, that we have to choose the initial starting time t_0 with care so as to capture the behaviour in the dynamical window, rather than the uninteresting regimes before and after it. We have therefore chosen the initial condition (2.7) with $L_0 = 0.07$ and so our simulations commence at $t_0 = 490$. For this case the smoothing turnoff time is $T = 100$. The value of L_0 is chosen because it is sufficiently close to $L_{\text{cat}} = 0.113$ where we have observed resonant behaviour for smaller Reynolds numbers. However it is still small enough so that any transient behaviour from the initial condition can die away and we have a smooth transition to the dynamical window in figure 11. This figure plots $\omega_{\text{or}}(t)$ for $A = 0$, 0.001, 0.0025, 0.005, 0.01 and 0.02 numbered 1 to 6 respectively.

In figure 11, and additionally in figure 12, where we plot (a) $\max(|\omega_2|)$, (b) $\sigma(t)$ and (c) $\log|Q_2(t)|$ against τ, we see similar results as for the smaller Reynolds number cases in figures 7–10. The results for $A = 0.001$, 0.0025 and 0.005 (curves 1–3) are relatively low amplitude results ($R_{\text{eff}} \simeq 3$, 12.5 and 35 respectively) and the rapid decay occurs at the end of the values of τ considered and beyond. This said however, the dynamical resonant
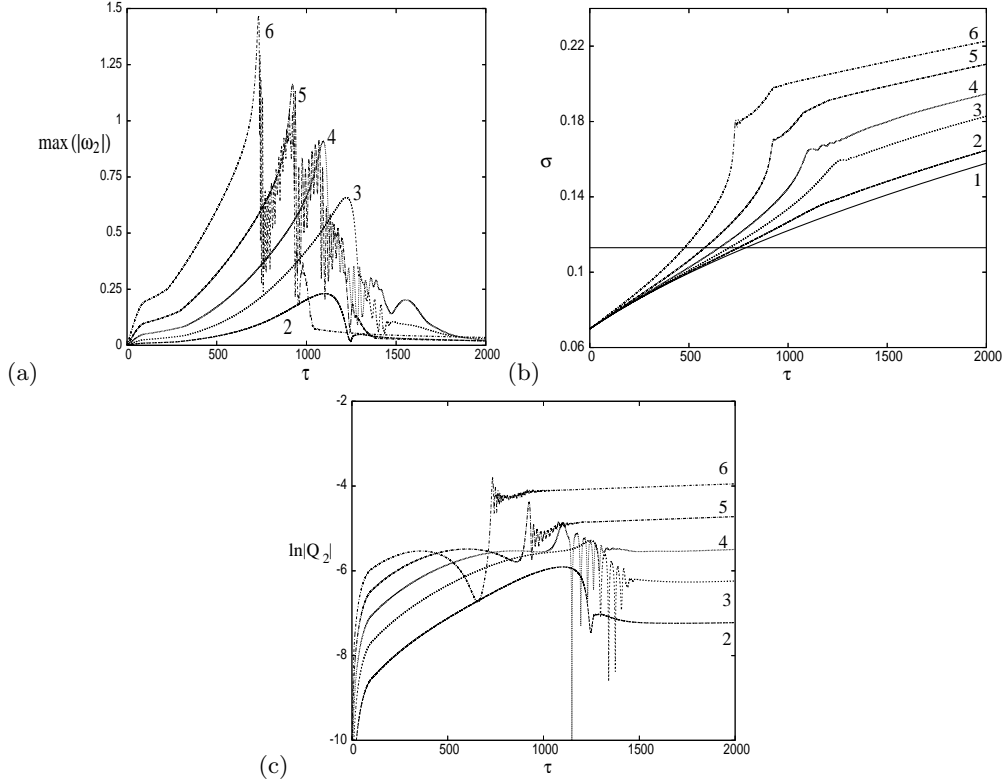
FIGURE 12. Plot of (a) $\max(|\omega_2|)$, (b) σ and (c) $\log|Q_2|$ against τ for $R = 10^5$ and $A = 0.001$, 0.0025, 0.005, 0.01 and 0.02 numbered 2 to 6 respectively. Panel (b) also includes the $A = 0$ result given by (2.9) this is numbered 1. The horizontal line in (b) corresponds to the resonant value $\sigma = L_{\text{cat}}$ in (3.5)

effect is captured in this range of τ for each of these amplitudes. This is examined further in §5.2. For the cases $A = 0.01$ and 0.02 (curves 4 and 5) the effective Reynolds number is much larger ($R_{\text{eff}} \simeq 100$ and 283) and the rapid drop in ω_{or} observed occurs within our dynamical window.

For the moment we note that for all results with $A \neq 0$ we see that the point at which the horizontal resonance line $\omega_{\text{or}} = \omega_{\text{cat}}$ from (3.5) first crosses each curve corresponds to the point where the results begin to separate from the $A = 0$ result and the point at which $\max(|\omega_2|)$ reaches its maximum value in figure 12(a). This corresponds to the resonance occurring with $r_{\text{ext}} = r_{\text{cat}}$ and not with $r_{\text{ext}} = r_{\text{qm}}$ which would occur at $\omega_{\text{or}} = \omega_{\text{qm}}$ in (3.6). This confirms the relevance of the inviscid radius r_{cat}, and corresponding frequency α_{cat}, at which infinitesimal cat's eyes can form, computed by Le Dizès (2000).

The difference between the diagnostics plotted in figure 12 for $R = 10^5$ compared to the lower Reynolds number versions in figures 9–10 is the inclusion of fine scale structure. In the low Reynolds number figures this structure is quickly damped out by viscosity and so is not observed. This structure is due to the rapid advection of vorticity around the cat's eyes that have been generated.

5.2. *Weak forcing amplitudes $A = 0.001$, 0.0025*

In figure 13 we plot the vorticity field $\omega(r, \theta, t)$ for a strain amplitude $A = 0.0025$ at times $\tau = 600$ to 1600 in increments of 200. This corresponds to curve 3 in figures 11
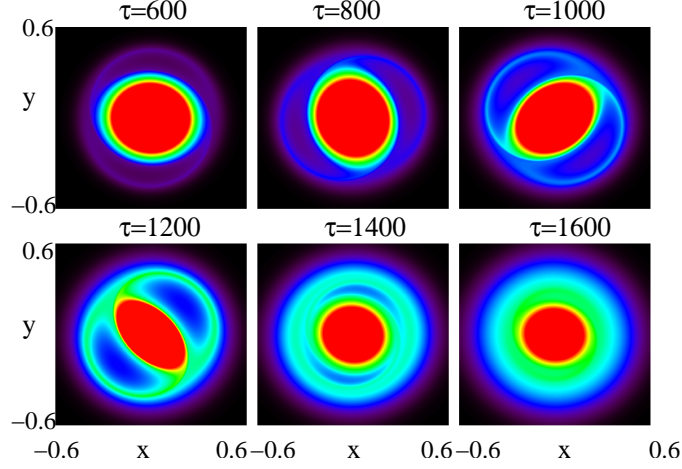
FIGURE 13. Plot of $\omega(r, \theta, t)$ for the case $R = 10^5$ and $A = 0.0025$ at times $\tau = 600, 800, 1000,$ 1200, 1400 and 1600 with $t_0 = 490$. The vorticity is capped at $\omega = 2$; red indicates regions of high vorticity and black regions of low vorticity. Note in each panel the vorticity is rescaled so red indicates the maximum vorticity of that panel.
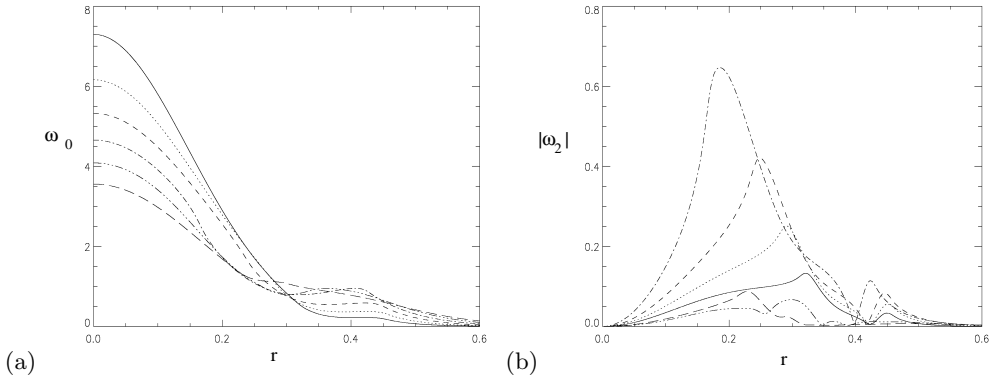

FIGURE 14. Plot of (a) $\omega_0(r, t)$ and (b) $|\omega_2(r, t)|$ against r for the case $R = 10^5$ and $A = 0.0025$ at times $\tau = 600, 800, 1000, 1200, 1400$ and 1600 with the same line style order as figure 4.

and 12, which is the second smallest strain amplitude considered in this study. Although this amplitude is approximately the same as the smallest non–zero value used in figures 6, 7 and 8, the effective Reynolds number is now much larger, with $R_{\text{eff}} = 12.3$, and so results are typical of a large Reynolds number R for the whole vortex, but moderate or small effective Reynolds number R_{eff} in the critical layer. The resulting basic vorticity profile $\omega_0(r, t)$ and first Fourier harmonic $|\omega_2(r, t)|$ for these panels are plotted in figures 14(a) and 14(b) respectively.

In figure 13 we see that for $\tau = 600$ the vortex is approximately axisymmetric; the corresponding $\omega_0(r, t)$ (figure 14, solid) has an homogenized region at $r \simeq 0.4$ and $|\omega_2(r, t)|$ has a double peaked structure with peaks at $r \simeq 0.35$ and $r \simeq 0.45$. By $\tau = 800$ the vortex core in figure 13 has become slightly elliptical in shape and two very weak filament lines can be seen to extend from the edge of the core, this is when ω_{or} dips in figure 11 and is very close to the threshold value of ω_{cat}. The dotted line in figure 14 shows that this time is around the time of the increased diffusion of vorticity at the origin: the flat region has moved slightly towards $r = 0$ and and both peaks of $|\omega_2(r, t)|$ have also increased
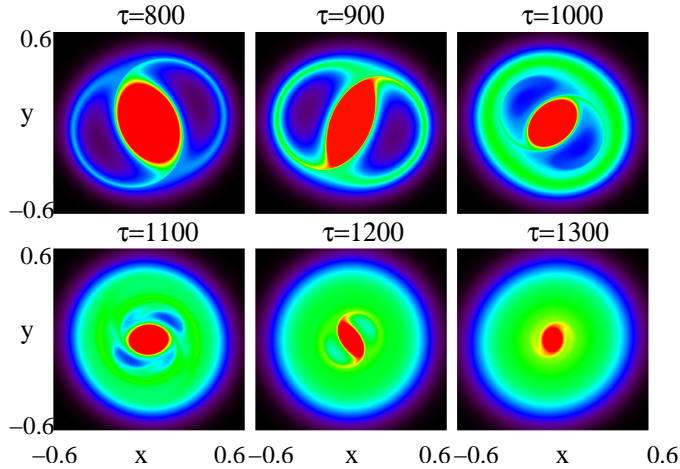
M. R. Turner and Andrew D. Gilbert

FIGURE 15. Plot of $\omega(r, \theta, t)$ for the case $R = 10^5$ and $A = 0.01$ at times $\tau = 800, 900, 1000, 1100, 1200$ and 1300 with $t_0 = 490$. The vorticity is capped at $\omega = 2$; red indicates regions of high vorticity and black regions of low vorticity. Note in each panel the vorticity is rescaled so red indicates the maximum vorticity of that panel.

in magnitude. At $\tau = 1000$ (dashed line in figure 14) the spiral arms are beginning to emanate from the vortex in figure 13 and the magnitude of the peaks in $|\omega_2|$ continue to increase until they reach their maximum value at $\tau = 1200$ (dot–dashed line). This corresponds to the spiral filaments combining with the vortex again in real space. From this point the peak in $|\omega_2(r, t)|$ decreases in value and the homogenized region of vorticity of $\omega_0(r, t)$ moves towards the origin in figure 14(a). This corresponds to the homogenizing of vorticity in the cat's eyes to give the elliptical vortex structure in figure 13.

5.3. *Larger amplitudes*

As the external amplitude A is increased, the rapid drop in vorticity value at the origin $\omega_{\mathrm{or}}(t)$ becomes more pronounced, we consider the run with $A = 0.01$, which is curve 5 in figures 11 and 12. Figures 15 and 16 show $\omega(r, \theta, t)$ along with $\omega_0(r, t)$ and $|\omega_2(r, t)|$ respectively, for $A = 0.01$ from $\tau = 800$ to 1300 in increments of 100. As in the earlier $A = 0.0025$ case, the figures indicate that $\omega_{\mathrm{or}}(t)$ cutting the resonant value ω_{cat} at $\tau \simeq 800$ is the point at which the spiral filaments reconnect with the vortex and begin to strengthen forming clear recirculating cat's eyes in the vorticity field. From figure 18 this is also the time at which the basic profile $\omega_0(r, t)$ first develops a local maximum at $r \simeq 0.45$.

  Once these spiral filaments have reattached, the core of the vortex becomes more elliptical ($\tau = 900$) and the strength of the filaments continue to grow ($\tau = 1000$). Figure 16(a) shows that $\omega_0(r, t)$ has a flat region at $r \simeq 0.4$ for $\tau = 800$ where the rapid decrease in ω_{or} begins to occur, but at $t = 900$, $\omega_0(r, t)$ (dotted line) now has a clear local maximum at $r \simeq 0.45$. This local maximum grows and moves towards the core for $\tau = 1000$ and $\tau = 1100$ and this indicates a possible reason for the resonant feedback of the nonlinear terms: the maximum has moved so that now $\omega_0'(r_{\mathrm{cat}}, t) > 0$. A positive gradient of vorticity in the critical layer is generally destabilising, from the asymptotic study of Balmforth *et al.* (2001), and this is presumably what leads to the rapid increase in $|\omega_2(r, t)|$ seen in figure 16(b); this in turn halts the further spread of the vortex.

  As we increase the amplitude of the strain to $A = 0.02$ with $R_{\mathrm{eff}} = 282.2$, the largest used in this study, we see a strange feature in the vorticity field, which is plotted from
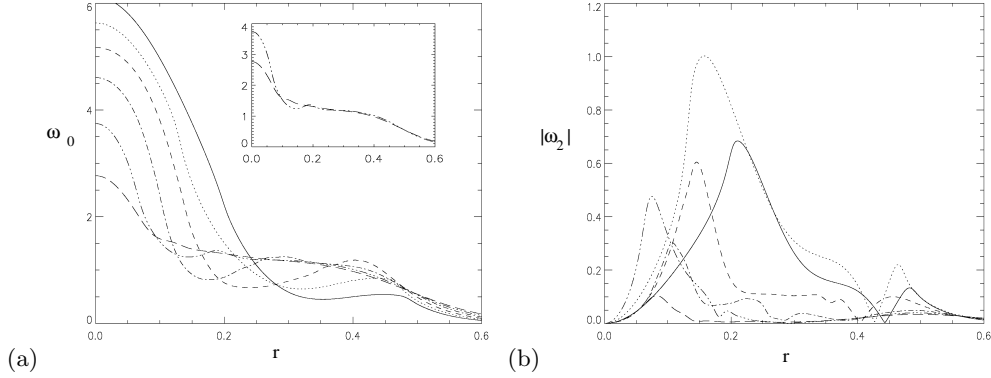
FIGURE 16. Plot of (a) $\omega_0(r,t)$ and (b) $|\omega_2(r,t)|$ against r for the case $R = 10^5$ and $A = 0.01$ at times $\tau = 800, 900, 1000, 1100, 1200$ and 1300 with $t_0 = 490$ and the same line style order as figure 4. The insert in panel (a) shows the $\tau = 1000$ and 1100 results separately for clarity.
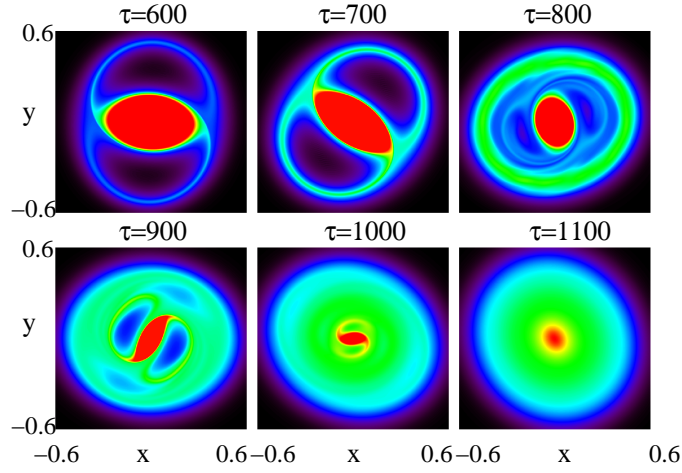

FIGURE 17. Plot of $\omega(r,\theta,t)$ for the case $R = 10^5$ and $A = 0.02$ at times $\tau = 600, 700, 800, 900, 1000$ and 1100 with $t_0 = 490$. The vorticity is capped at $\omega = 2$; red indicates regions of high vorticity and black regions of low vorticity. Note in each panel the vorticity is rescaled so red indicates the maximum vorticity of that panel.

$\tau = 600$ to 1100 in increments of 100 in figure 17. Initially this simulation is much like the other simulations in this section with spiral filaments of vorticity beginning to strengthen at $\tau = 600$ and reaching their maximum value at $\tau = 700$. The vorticity then homogenizes in the vortex at $\tau = 800$, but at $\tau = 900$ we see the intriguing feature of two sets of cat's eyes being visible in the vortex, although one set is much weaker than the other. By $\tau = 1100$ both sets of cat's eyes have vanished and the vortex again axisymmetrizes as in the other simulations in the section.

To understand this behaviour further we study the sequence of plots of $\omega_0(r,t)$ and $|\omega_2(r,t)|$ against r in figure 18. At $\tau = 600$ the ω_0 profile has a flat region at $r \simeq 0.4$, but by $\tau = 800$ a local maximum now occurs around this value. This maximum peak moves towards the core, but then interacts with the vorticity that has spread from the core. At $\tau = 900$ the $\omega_0(r,t)$ profile now has two local maxima at $r \simeq 0.28$ and $r \simeq 0.37$. The existence of this extra maximum appears to increase the spreading of vorticity further,
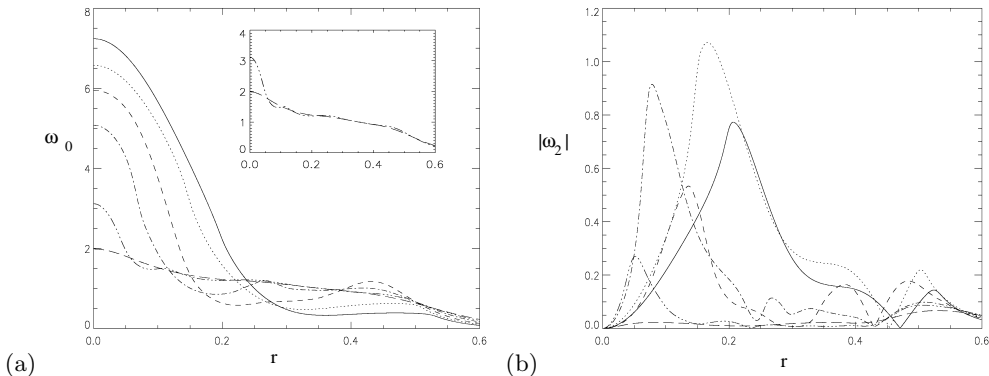
FIGURE 18. Plot of (a) $\omega_0(r,t)$ and (b) $|\omega_2(r,t)|$ against r for the case $R = 10^5$ and $A = 0.02$ at times $\tau = 600, 700, 800, 900, 1000$ and 1100 with $t_0 = 490$ with the same line style order as figure 4. The insert in panel (a) shows the $\tau = 900, 1000$ and 1100 results separately for clarity.

as the remnant core left in the $\tau = 1100$ panel in figure 17 is much smaller than the core in the $\tau = 1300$ panel of figure 15.

It is possible to extend our runs to higher values of the Reynolds number, but preliminary results show that these are in qualitative agreement with the $R = 10^5$ results we have presented, so we do not investigate this further here.

6. Conclusions and discussion

In this paper we studied how a viscously spreading Gaussian vortex evolves when placed in a rotating strain field which has constant angular velocity α_{ext} and a constant amplitude $\hat{A}$. By choosing suitable non–dimensional variables, this study becomes a problem with two parameters, the Reynolds number R and the non–dimensional amplitude $A = \hat{A}/\alpha_{\text{ext}}$ for $m = 2$. Equivalently we have the two competing parameters of the Reynolds number R which controls the global evolution of the spreading vortex, and the effective Reynolds number R_{eff} in (3.3) which is the appropriate value for fluid motions within the critical layer or cat's eyes. Varying these parameters yields a complex picture, particularly at large R_{eff}. Essentially, since R controls the global spread of the vortex, it controls the time the vortex spends in any kind of resonance with the external forcing, the width of the dynamical window. During such a resonance phenomenon, though, in which cat's eyes advect vorticity and change the profile, the appropriate Reynolds number is R_{eff}.

For $R = 10^3$, we found that the external strain field generates cat's eye topology in the flow field, and as the cat's eyes move towards the centre of the vortex there is a resonant effect which causes a rapid rearrangement of vorticity, including a rapid drop in the value of vorticity at the origin. Once the vortex has spread enough so that the strain field no longer generates a critical radius r_{ext} in the vortex, the elliptical vortex spreads as t^{-1} (Rhines and Young, 1983). As the Reynolds number R is increased we found that for very low external forcings, and so $R_{\text{eff}} \ll 1$, the response is similar to that given in the linear study of Lingevitch and Bernoff (1995). It is also observed that this rapid drop in ω_{or} occurs when vorticity forms into cat's eye structures around the time when r_{ext} takes the value in (3.4): this is when the external strain frequency corresponds to the radius at which an unforced Gaussian vortex supports infinitesimally thin viscous cat's eyes. The rapid decay ends when the cat's eyes vanish from the vortex.

For large Reynolds numbers ($R = 10^5$) and large A (and so large R_{eff}) there is a strong

resonant effect that occurs around the time when $r_{\text{ext}} \simeq r_{\text{cat}}$, producing nonlinear behaviour. Although the vortex is only approximately Gaussian, this criterion works well. This appears to be because what controls the value of r_{cat} (and r_{qm}) is the main, coherent part of the vortex which takes an approximately Gaussian form: the less organised vorticity near the periphery, which is wound into the cat's eyes, is less important. This makes $\omega_{\text{or}}(t)$, the amplitude of the vortex core, the best measure of this threshold. The formation of broad cat's eyes generates a big region into which the vorticity can spread rapidly. This rapid spreading of the vortex, coupled with the large amplitude of the forcing, generates vorticity fields where we observe two sets of cat's eyes. We also observe in the vorticity field plots of figure 17 that the vorticity is strongly mixed at the periphery of the vortex, akin to the surf zones seen in Charlton *et al.* (2004), and one of our future objectives is to quantify this mixing.

We noted that the quasi–mode radius r_{qm} has no obvious dynamical influence on the resonant behaviour of the vortex. This clears up the discussion from Turner and Gilbert (2007): here a vortex was forced at the external frequency α_{qm} and thresholds were obtained for the formation of cat's eyes at the radius r_{qm}. However these cat's eyes are of finite width, and it is more natural to force at the frequency α_{cat} (called α_{LD} in Turner and Gilbert (2007)) for which the vortex can support cat's eyes of infinitesimal width at the corresponding radius (Le Dizès, 2000). It is at this frequency α_{cat} that we see the resonant response in our forced, spreading vortex.

This study focused on a very simple, deterministic forcing of just one frequency. We note that the picture is rather more complex than the case of a steady external strain field $\alpha_{\text{ext}} = 0$: in that case when the vortex spreads enough to interact strongly with the external strain, vorticity is stripped to infinity in the open, strain field topology, and the vortex is destroyed. In our case the topology of cat's eyes embedded in the flow means that any vorticity in the cat's eyes remains close to the vortex and recirculates. This gives the possibility of complicated time–dependence and spatial structure, as we have observed. We note that in applications, having an external strain with just one frequency is somewhat idealised, and one would typically expect several frequencies, or a random time dependence containing a whole spectrum of frequencies; this is currently under investigation (Turner *et al.*, 2009).

References

Balmforth, N. J., Llewellyn Smith, S. G., and Young, W. R. (2001). Disturbing vortices. *J. Fluid Mech.*, **426**, 95–133.

Bassom, A. P. and Gilbert, A. D. (1998). The spiral wind-up of vorticity in an inviscid planar vortex. *J. Fluid Mech.*, **371**, 109–140.

Briggs, R. J., Daugherty, J. D., and Levy, R. H. (1970). Role of Landau damping in crossed-field electron beams and inviscid shear flow. *Phys. Fluids*, **13**, 421–432.

Charlton, A. J., O'Neill, A., Lahoz, W. A., and Berrisford, P. (2004). The splitting

of the Stratospheric vortex in the southern hemisphere, September 2002: Dynamical evolution. *J. Atmospheric Sci.*, **62**, 590–602.

Dritschel, D. G. (1995). A general theory for two-dimensional vortex interactions. *J. Fluid Mech.*, **293**, 269–303.

Dritschel, D. G. and Waugh, D. W. (1992). Quantification of the inelastic interaction of unequal vortices in two–dimensional vortex dynamics. *Phys. Fluids*, **4**(8), 1737–1744.

Haberman, R. (1972). Critical layers in parallel flows. *Stud. Appl. Maths*, **51**, 139–161.

Hall, I. M., Bassom, A. P., and Gilbert, A. D. (2003). The effect of fine structure on the stability of planar vortices. *Eur. J. Mech. B Fluids*, **22**(2), 179–198.

Hosokawa, I. and Yamamoto, K. (1989). Fine structure of a directly simulated isotropic turbulence. *J. Phys. Soc. Japan*, **58**, 20–23.

Jiménez, J., Moffatt, H. K., and Vasco, C. (1996). The structure of the vortices in freely decaying two-dimensional turbulence. *J. Fluid Mech.*, **313**, 209–222.

Koh, T.-Y. and Plumb, R. A. (2000). Lobe dynamics applied to barotropic Rossby-wave breaking. *Phys. Fluids*, **12**(6), 1518–1528.

Le Dizès, S. (2000). Non-axisymmetric vortices in two-dimensional flows. *J. Fluid Mech.*, **406**, 175–198.

Lingevitch, J. F. and Bernoff, A. J. (1995). Distortion and evolution of a localized vortex in an irrotational flow. *Phys. Fluids*, **7**(5), 1015–1026.

Lundgren, T. S. (1982). Strained spiral vortex model for turbulent fine structure. *Phys. Fluids*, **25**(12), 2193–2203.

Mariotti, A., Legras, B., and Dritschel, D. G. (1994). Vortex stripping and the erosion of coherent structures in two-dimensional flows. *Phys. Fluids*, **6**(12), 3954–3962.

Moffatt, H. K., Kida, S., and Ohkitani, K. (1994). Stretched vortices—the sinews of turbulence; large-Reynolds-number asymptotics. *J. Fluid Mech.*, **259**, 241–264.

Polvani, L. M. and Plumb, R. A. (1992). Rossby wave breaking, microbreaking, filamentation, and secondary vortex formation: the dynamics of a perturbed vortex. *J. Atmospheric Sci.*, **49**(6), 462–476.

Provenzale, A. (1999). Transport by coherent barotropic vortices. In *Annual review of fluid mechanics, Vol. 31*, volume 31 of *Annu. Rev. Fluid Mech.*, pages 55–93. Annual Reviews, Palo Alto, CA.

Rhines, P. B. and Young, W. R. (1983). How rapidly is a passive scalar mixed within closed streamlines? *J. Fluid Mech.*, **133**, 133–145.

Schecter, D. A., Dubin, D. H. E., Cass, A. C., Driscoll, C. F., Lansky, I. M., and O'Neil, T. M. (2000). Inviscid damping of asymmetries on a two-dimensional vortex. *Phys. Fluids*, **12**(10), 2397–2412.

Thuburn, J. and Lagneau, V. (1999). Eulerian mean, contour integral, and finite–amplitude wave activity diagnostics applied to a single–layer model of the winter Stratosphere. *J. Atmospheric Sci.*, **56**(5), 689–710.

Turner, M. R. and Gilbert, A. D. (2007). Linear and nonlinear decay of cat's eyes in two-dimensional vortices, and the link to Landau poles. *J. Fluid Mech.*, **593**, 255–279.

Turner, M. R., Gilbert, A. D., and Bassom, A. P. (2008). Neutral modes of a two-dimensional vortex and their link to persistent cat's eyes. *Phys. Fluids*, **20**(2), 027101–1–027101–10.

Turner, M. R., Bassom, A. P., and Gilbert, A. D. (2009). Diffusion and the formation of vorticity staircases in randomly strained two–dimensional vortices. *J. Fluid Mech.*, **638**, 49–72.